Direct Observation of Feedout-Related Mass Oscillations in Plastic Targets

Y. Aglitskiy,[1] A. L. Velikovich,[2] M. Karasik,[2] V. Serlin,[2] C. J. Pawley,[2] A. J. Schmitt,[2] S. P. Obenschain,[2]
A. N. Mostovych,[2] J. H. Gardner,[3] and N. Metzler[1]

[1]*Science Applications International Corporation, McLean, Virginia 22150*
[2]*Plasma Physics Division, Naval Research Laboratory, Washington, D.C. 20375*
[3]*Laboratory for Computational Physics and Fluid Dynamics, Naval Research Laboratory, Washington, D.C. 20375*
(Received 9 August 2001; published 6 December 2001)

"Feedout" means the transfer of mass perturbations from the rear to the front surface of a driven target. When a planar shock wave breaks out at a rippled rear surface of the target, a lateral pressure gradient drives sonic waves in a rippled rarefaction wave propagating back to the front surface. This process redistributes mass in the volume of the target, forming the feedout-generated seed for ablative Rayleigh-Taylor (RT) instability. We report the first direct experimental observation of areal-mass oscillation associated with feedout, followed by the onset of exponential RT growth.

One of the sources of the initial mass nonuniformity for the Rayleigh-Taylor (RT) perturbation growth in laser fusion targets is the roughness of the inner surface of the target [1,2]. The process that transfers mass perturbation from the inner to the outer surface of the target, where the RT instability develops, is called feedout. In planar geometry, the RT growth begins after a planar shock wave initiated at the smooth front surface of the target breaks out at its ripped rear surface, and a rippled rarefaction wave reflected from it reaches the front surface. The shock-rarefaction transit time is shorter for the thinner parts of the target, which start accelerating earlier. If the wavelength of the rear-surface ripples λ is sufficiently long compared to the shock-compressed target thickness L_s ($\lambda \gg 2\pi L_s$; see Ref. [3]), then the thinner parts of the target also experience a higher acceleration under the same driving pressure because of their lower areal mass. As a result, these thinner parts evolve into bubbles, propagating ahead and dumping more of their mass into the spikes that trail behind, as demonstrated in theoretical work [4] and then observed experimentally [5].

What if the perturbation wavelength is not that long? Then, as explained in [3], lateral mass redistribution in a reflected rippled rarefaction wave cannot be neglected. When a shock wave first breaks out at the valleys of the rippled rear surface, expansion and decompression start from there, whereas the pressure in the shock wave still propagating towards the peaks remains at the constant postshock value. The resulting lateral pressure gradient starts driving mass from peaks to valleys, decreasing the pressure near the peaks and increasing it near the valleys, at some point overshooting the pressure equilibrium and building up a reversed pressure gradient. These sonic oscillations of areal mass in a rippled rarefaction wave have been first described in Ref. [6].

It is informative to compare oscillations of areal mass in a shock wave (due to the ripples at the front surface of the target), and in a rarefaction wave (due to the ripples at the rear surface of the target), as in the experiments [7,8]

and [2], respectively. Figure 1 presents the comparison as given by analytical small-amplitude theory applied to a planar layer of ideal gas with $\gamma = 5/3$, rippled from either front or rear side [3,9,10]. Here the areal mass variation amplitude δm is expressed in units $\rho_0 a_0$ (where ρ_0 is the preshock density, a_0 is the initial ripple amplitude), $k = 2\pi/\lambda$ is the ripple wave number, and a_s is the postshock speed of sound. The origin of time $t = 0$ for the "shock" curves corresponds to the instant when a constant intensity shock wave is launched at the rippled surface of the target, and for the "rarefaction" curve—to the shock breakout at the rippled rear surface of the target. The shock curves account for contributions to the mass variation inside the target, from the rippled shock front and the nonuniform postshock flow. These curves do not show the contribution from the rippled front surface, or
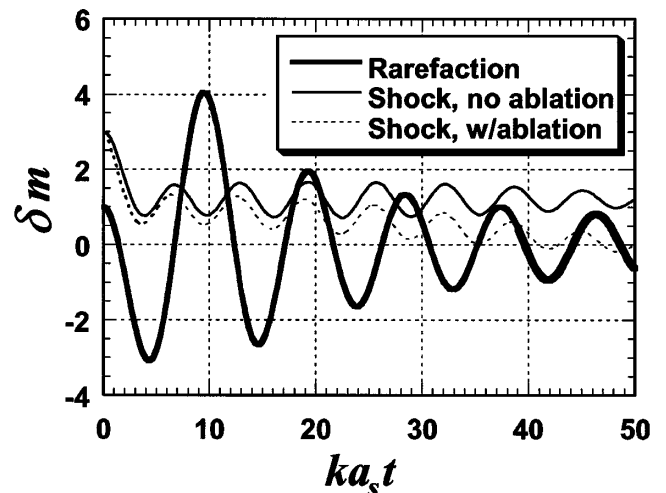

FIG. 1. Time history of normalized mass variation in a planar target caused by a rippled rarefaction wave and a rippled shock wave (small-amplitude theory). Initial amplitudes of the front and rear surface ripples are the same; the time origin for the rarefaction curve is shifted to the shock breakout at the rippled rear surface.

ablation front. The "no ablation" curve is plotted using the boundary condition that assumes the rippled front surface to be a material interface, where a constant pressure is maintained. The curve "with ablation" treats the front surface as an ablation front, where the Sanz-Piriz boundary conditions are satisfied [10,11]; our example refers to a DT target with a front ripple wavelength 30 μm and ablation-front-to-blowoff-plasma density ratio 8.95, all other parameters being the same as in [9]. We see that lateral variation of areal mass is much more pronounced in a rippled rarefaction wave than in a rippled shock wave. In particular, phase reversal of areal mass—which means that the initially thinner and thicker parts of the target become more and less massive, respectively—cannot happen in a rippled shock wave. The theory, however, predicts it to occur repeatedly in a rippled rarefaction wave, with first mass perturbation phase reversal occurring shortly after the shock breakout; see Fig. 1. Equations (18) and (23) of [3] yield an estimate for the time interval between the shock breakout and the first phase reversal:

$$t_1 = \frac{[2(3\gamma - 1)]^{1/2}}{(2\gamma)^{1/2} + (\gamma - 1)^{1/2}} \times \frac{\lambda R t_s}{2\pi(R - 1)^{1/2} L_0}$$

$$\cong \frac{\lambda}{\pi L_0} t_s, \tag{1}$$

where R is the shock compression ratio, L_0 is the preshock target thickness, and t_s is the shock transit time. Parameters γ and R enter (1) separately, as the ideal gas equation of state might be applicable only to the target material when it expands after the shock passage [12]. The γ-dependent numerical coefficient in (1) is close to unity; for strong shocks, $R = 1.5$ to 4, the R-dependent factor is $\cong 2$. In our estimates below, we assume for multi-Mbar shocks $\gamma = 5/3$, $R = 4$.

After the rippled rarefaction wave breaks out at the front surface, the target starts accelerating, which triggers the RT growth. It begins at the thinner parts of the target, where the rippled leading edge arrives first, and continues with the initial perturbation phase, further decreasing the areal mass in the initially thinner parts. When the long-wavelength condition is not satisfied, the rarefaction transit time exceeds t_1, and this growth has to compete against the lateral mass redistribution in a rippled rarefaction wave: the initially thinner parts become more massive. In our experimental conditions, the leading edge of the rippled rarefaction wave first arrives to the front surface where the target was initially thinner. This triggers a RT perturbation growth in phase with the initial mass distribution, transferring the mass from initially thinner to initially thicker parts of the target. The RT growth eventually prevails over the rippled rarefaction wave effects, and the mass variation amplitude reverses phase again, after which δm continues to increase.

Some of the effects discussed here have been detected in experiments and simulations of Ref. [2], where a hohlraum drove an 85 μm thick Al target rippled on the rear surface

($\lambda = 50$ μm). For a high-intensity 2.2 ns long hohlraum pulse ([2], Fig. 7), the first phase reversal was observed [for $t_s = 2$ ns, Eq. (1) gives $t_1 = 0.46$ ns close to the observed and simulated values], and the second one was predicted by the LASNEX simulation, but not observed. For a low-intensity 4.5 ns long hohlraum pulse ([2], Fig. 9), the LASNEX simulation again predicted two phase reversals (for $t_s = 2.5$ ns, we find $t_1 = 0.58$ ns, again close to the simulated value) and some growth with initial phase; only the latter was actually observed.

We report here the first direct observation of the whole perturbation evolution caused by feedout: a shock breakout at the rippled rear surface, two phase reversals, and a subsequent RT growth. Our experiments were performed with the Nike KrF laser [13] ($\lambda_L = 248$ nm). The 4 ns long laser pulse (~1400 J in 37 overlapping beams) was focused to a spot 750 μm in diameter FWHM, producing intensity up to ~8×10^{13} W/cm^2. The time-averaged rms spatial variation for a single beam has been measured to be 1%–2%; hence the feedout-related evolution of perturbations was not obscured by the laser imprint effects.

The diagnostic setup for the feedout measurements was the same as used in our experiments on ablative Richtmyer-Meshkov instability and was described in detail in a separate paper [8]. It is a modification of the Nike monochromatic x-ray imaging system based on Bragg reflection from spherically curved crystals [14]. The He-like resonance line ($h\nu = 1.86$ keV), selected by a spherically curved quartz crystal from the radiation of a silicon backlighter illuminated the main target for about 5 ns. The monochromatic image of the target was projected on the entrance slit of the x-ray streak camera with a positioning accuracy that corresponds to 30 μm on the target. The streak records were taken with a time resolution of 170 ps. As in Ref. [8], spatial resolution was provided in one relevant direction, along the wave vector of the sine-wave ripple on the rear surface of the target. The large flat top (400 μm) of the laser focal spot and a large field of view (500 μm) give us more ripples available for Fourier transform analysis, thus ensuring confidence in determining mode amplitude. The Fourier amplitudes presented below are modulation transfer function (MTF)-corrected, the MTF at $\lambda = 30$ and 45 μm being 0.4 and 0.7, respectively. An experimental error bar for the mode amplitude measurement does not exceed ± 1 μm in most cases [8].

We used 40 to 60 μm thick CH targets rippled on the rear side. The initial ripple amplitudes and wavelengths were approximately either 1 and 30 μm, or 1.5 and 45 μm. These perturbation amplitudes were too high for observing linear RT growth: with $ka_0 = 0.42$ we were close to the nonlinear stage from the start. In the rippled rarefaction wave, however, perturbations of all wavelengths oscillate rather than grow exponentially. In our simulations, we verified that the higher harmonics, being initially small, remain small until the onset of the experimental RT growth.

Compared to Richtmyer-Meshkov and RT growth, feedout-related oscillations are much more difficult to
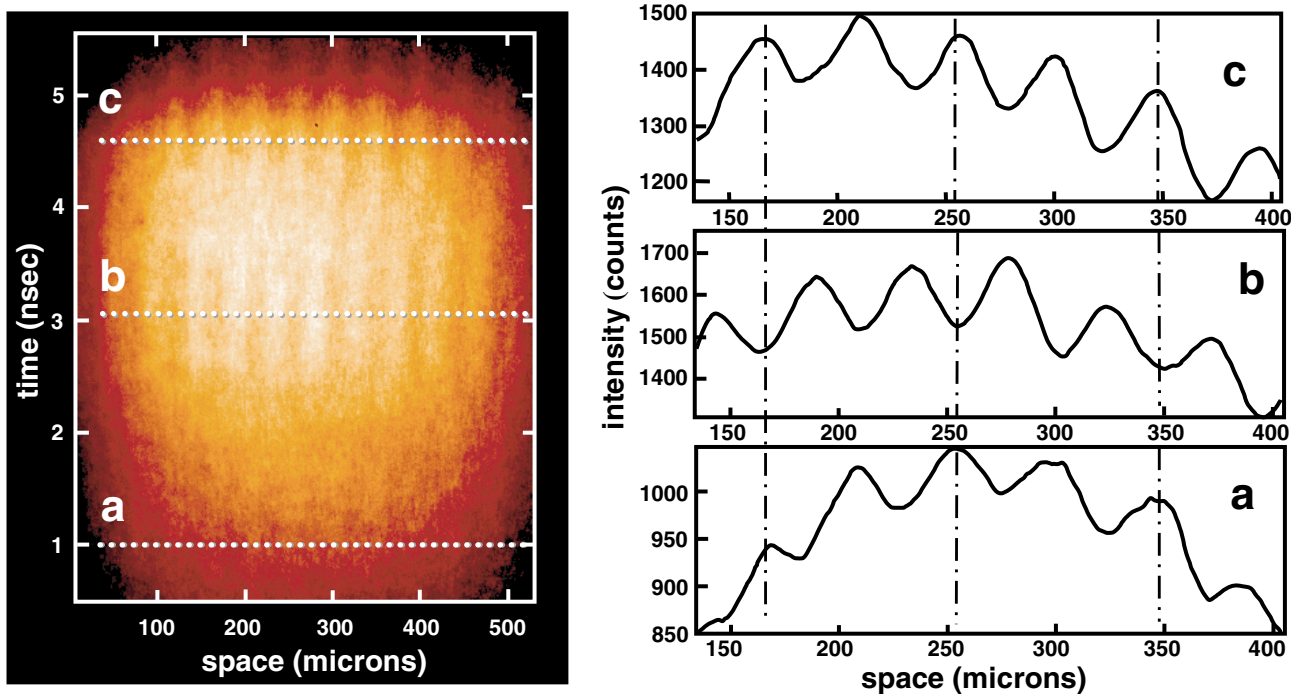
FIG. 2 (color).   Streak record (left) and its line-outs at three different times (right) for target thickness 60 μm, $\lambda = 46$ μm, and peak laser intensity 5×10^{13} W/cm^2. Two phase reversals are clearly seen on both the line-outs and the image.

observe since the areal mass amplitude is smaller than the initial one during most of the oscillation. However, as Fig. 2 demonstrates, we were still able to observe this oscillation thanks to the high contrast capability of our diagnostics. Shown is a streak record (left) taken with a target thickness 60 μm, $\lambda = 46$ μm, peak laser intensity 5×10^{13} W/cm^2, and its line-outs at three different times (right). The two phase reversals illustrated by the line-outs are clearly seen on the original streak record. The light and dark stripes that correspond to low and high areal masses, respectively, are seen at early time, and then disappear, as if at about $t = 2$ ns they were smeared out in a horizontal band ~ 0.5 ns wide. Then the stripes reappear, but the light and dark ones change places, indicating a 180° phase reversal, which occurs about the time predicted by Eq. (1) for $t_s = 1.5$ ns: here $t_1 = 0.4$ ns. Shortly after this, the RT growth in the positive direction (at the initial phase) begins, and the phase of areal mass modulation is reversed again, this time at about 4 ns. The growth is also clearly visible: dark and light stripes, representing peaks and valleys of areal mass distribution, respectively, become more pronounced at late time.

Figure 3 compares the oscillations observed in 40 and 60 μm targets with the same perturbation amplitude $a_0 = 1.5$ μm, wavelength $\lambda = 45$ μm, irradiated at the same peak intensity 5×10^{13} W/cm^2. The respective shock waves and reflected rarefaction waves have about the same velocities in both cases. The rarefaction transit time is 50% greater for a 60 μm target. In both cases, the lateral mass flow in a rippled rarefaction wave leads to a phase reversal of the mass perturbation pattern with respect to the original mass distribution. The maximum am-

plitude of the out-of-phase mass perturbation generated by a rippled rarefaction wave grows as the normalized transit time $ka_s t = 2\pi L_0 / \lambda R$ [3] is increased from 1.5 to 4.3; see Fig. 1. In contrast, the leading edge of the
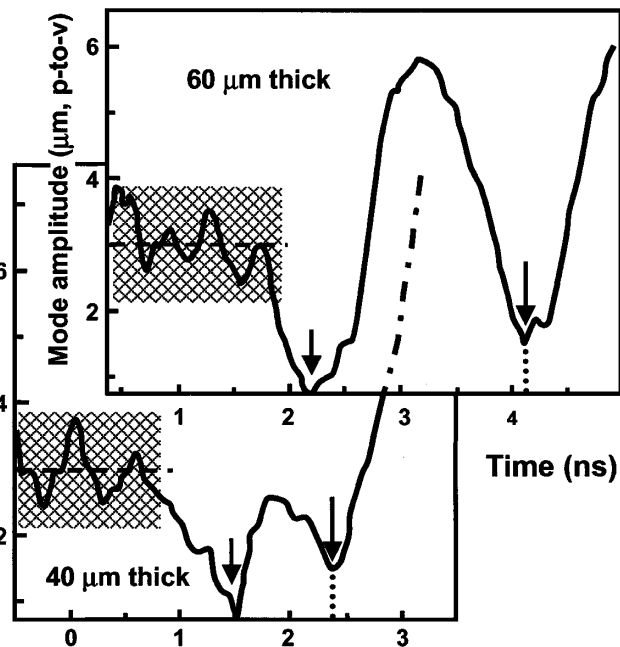

FIG. 3.   Peak-to-valley amplitudes of the dominant Fourier modes for 40 and 60 μm thick targets vs time. $2a_0 = 3$ μm, $\lambda = 45$ μm, and peak laser intensity 5×10^{13} W/cm^2. First and second phase reversals are marked on both pictures. The thickness of the shaded area corresponds to the experimental uncertainty of the mode amplitude measurement.
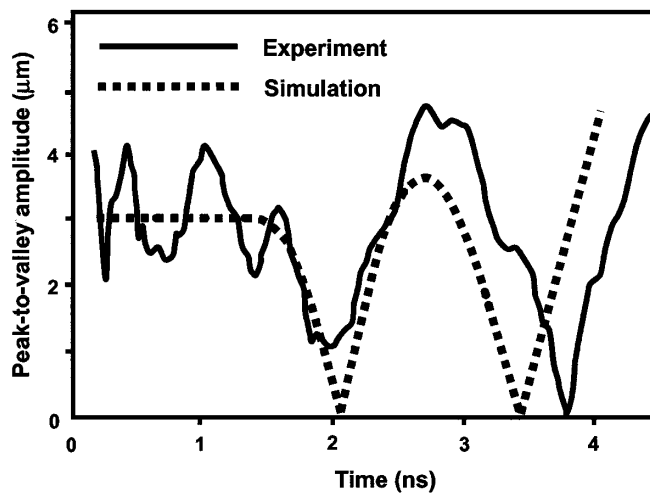
FIG. 4. Peak-to-valley amplitudes of the dominant Fourier modes for a 60 μm thick targets vs time. $2a_0 = 3$ μm, $\lambda = 45$ μm, and peak laser intensity 5×10^{13} W/cm^2. Solid line—experiment; dotted line—simulation.

rarefaction wave preserves the initial perturbation phase, and upon rarefaction breakout on the front, the RT growth is in phase with the initial perturbation. As the RT instability develops, the amplitude of mass variation first decreases, then its phase is reversed again, and it continues growing until the laser pulse ends and the target decompresses. The RT growth is seen to start earlier for the thinner target, as it should.

Figure 4 shows the data obtained for a 60 μm thick target with the same perturbation amplitude $a_0 = 1.5$ μm and wavelength $\lambda = 45$ μm, irradiated at the same peak intensity 5×10^{13} W/cm^2. Here $t_s = 1.5$ ns, $t_1 = 0.5$ ns calculated from (1) are again in agreement with the observation. This time history of the dominant mode is compared to a simulation performed in two dimensions (2D) using the FAST2D hydrocode developed at the Naval Research Laboratory [15]. Qualitatively, the simulation predicts exactly what we observe in all shots: two phase reversals, and then some RT growth. Quantitative agreement is also quite reasonable.

In summary, we have observed for the first time a distinct oscillation (two phase reversals) followed by the monotonic RT growth of areal mass variation in a feedout geometry. The osculation is due to the competition

between the lateral mass redistribution in a reflected rippled rarefaction wave, which reverses the phase of mass modulation, and the RT growth that starts where the target is initially thinner and tends to further decrease the areal mass there. The latter prevails in our experimental conditions, as well as in those of Ref. [2], resulting in exactly two phase reversals. A challenge for a future experiment is to observe *three* phase reversals, producing the RT bubbles where the target was initially thicker (cf. Ref. [3]). A challenge for a future simulation is to achieve a better quantitative agreement with our results. Finally, a challenge for the theory is to derive a relation between the initial rear surface ripple amplitude and the preexponential factor at the linear RT growth stage, generalizing the results of Ref. [4] for the case when two or more phase reversals take place.

[1] K. O. Mikaelian, Phys. Rev. A **31**, 410 (1985); W. J. Crauser *et al.,* Phys. Plasmas **3**, 2084 (1996); D. C. Wilson *et al.,* Phys. Plasmas **5**, 1953 (1998).
[2] D. P. Smitherman *et al.,* Phys. Plasmas **6**, 932 (1999).
[3] A. L. Velikovich *et al.,* Phys. Plasmas **8**, 592 (2001).
[4] R. Betti *et al.,* Phys. Rev. Lett. **81**, 5560 (1998).
[5] K. Shigemori *et al.,* Phys. Rev. Lett. **84**, 5331 (2000).
[6] A. L. Velikovich and L. Phillips, Phys. Fluids **8**, 1107 (1996).
[7] T. Endo, Phys. Rev. Lett. **74**, 3608 (1995).
[8] Y. Aglitskiy *et al.,* Phys. Rev. Lett. **87**, 265001 (2001).
[9] V. N. Goncharov, Phys. Rev. Lett. **82**, 2091 (1999).
[10] A. J. Schmitt *et al.,* Phys. Plasmas **8**, 2287 (2001).
[11] J. Sanz, Phys. Rev. Lett. **73**, 2700 (1994); A. R. Piriz *et al.,* Phys. Plasmas **4**, 1117 (1997).
[12] Ya. B. Zel'dovich and Yu. P. Raizer, *Physics of Shock Waves and High-Temperature Hydrodynamic Phenomena* (Academic Press, New York, 1966), Vol. 2.
[13] S. P. Obenschain *et al.,* Phys. Plasmas **3**, 2098 (1996).
[14] Y. Aglitskiy *et al.,* Appl. Opt. **37**, 5253 (1998).
[15] J. P. Boris and D. L. Book, J. Comput. Phys. **11**, 38 (1973); also see *Methods in Computational Physics* (Academic Press, New York, 1976), Vol. 16, p. 85–129.